Structure of a bacterial OapB protein with its OLE RNA target gives insights into the architecture of the OLE ribonucleoprotein complex

Yang Yang[a,b,1], Kimberly A. Harris[a], Danielle L. Widner[c], and Ronald R. Breaker[a,b,c,1]

[a]Department of Molecular, Cellular and Developmental Biology, Yale University, New Haven, CT 06520-8103, USA;
[b]Howard Hughes Medical Institute, Yale University, New Haven, CT 06520-8103, USA;
[c]Department of Molecular Biophysics and Biochemistry, Yale University, New Haven, CT 06520-8103, USA

[1]To whom correspondence may be addressed. Email: y.yang@yale.edu; ronald.breaker@yale.edu

Classification: Biology, Biophysics and Computational Biology

Keywords: alcohol toxicity | GNRA tetraloop | KOW motif | Mg^{2+} tolerance | noncoding RNA

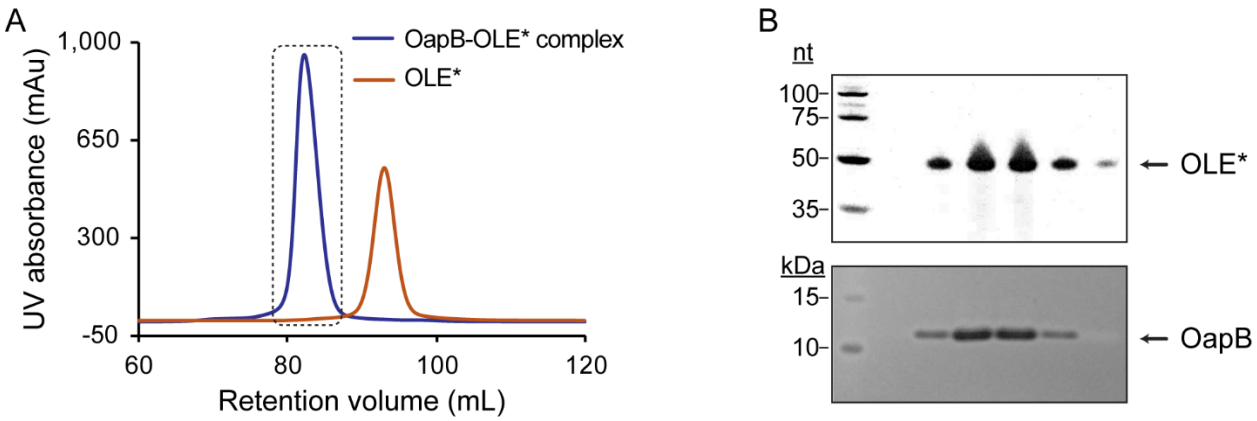

Figure S1. OapB-OLE* complex reconstitution. (*A*) Size-exclusion chromatography (SEC) profiles of OLE* alone (orange) and OapB-OLE* complex (blue). Due to lack of tryptophan residues in OapB, the peak corresponding to excessive OapB is not visible. (*B*) The SEC purification fractions in the dashed line box were resolved on denaturing polyacrylamide gels and stained with SYBR Gold for RNA or stained with Coomassie blue for protein. A denatured double-stranded DNA marker was used in the gel stained with SYBR Gold.

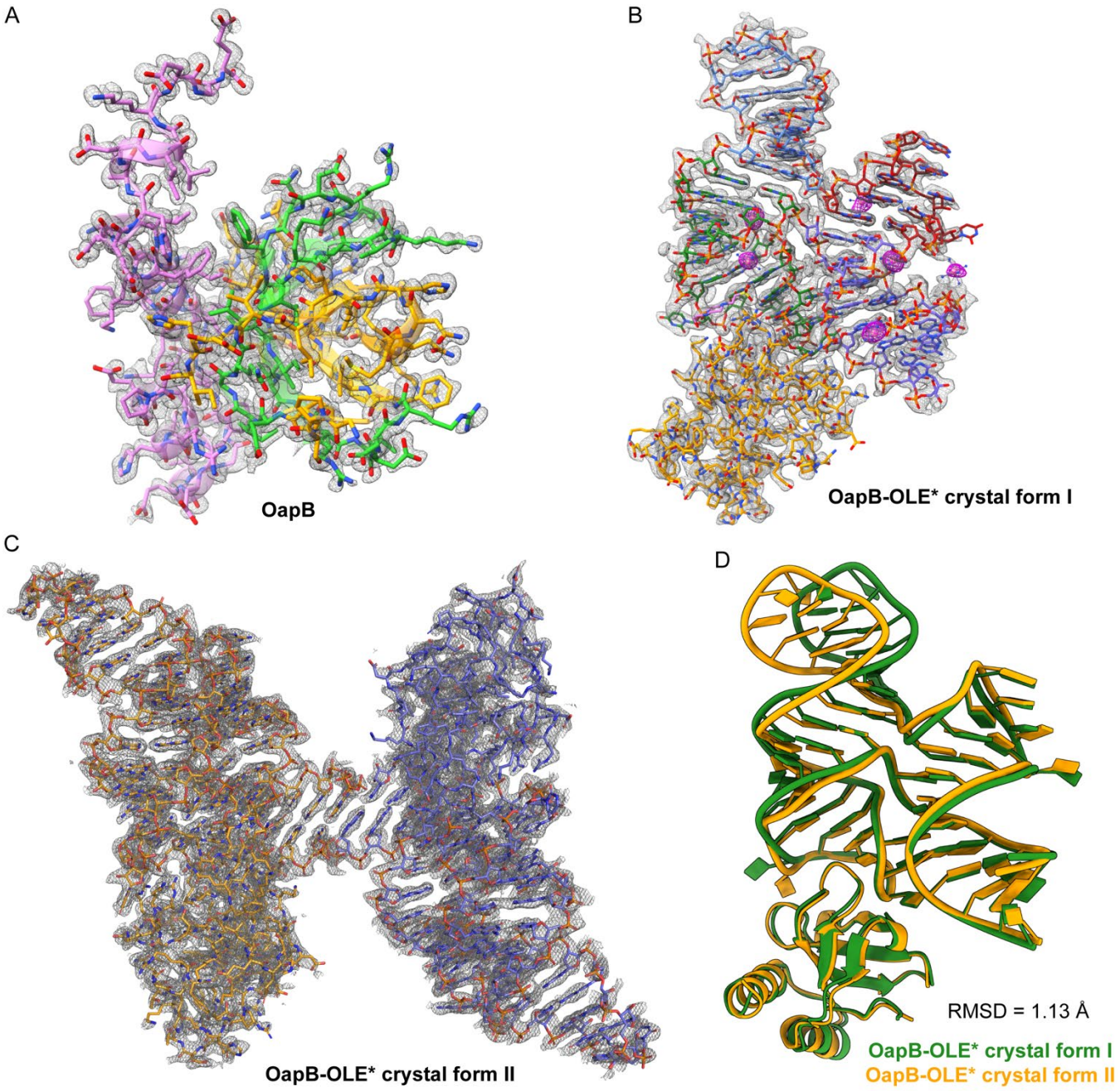
A
OapB
B
OapB-OLE* crystal form I
C
OapB-OLE* crystal form II
D
RMSD = 1.13 Å
OapB-OLE* crystal form I
OapB-OLE* crystal form II
E
A504
G577
G578
G503
G501
U499
C579
U502
R20
K51
R49
U498
R35
N56
N54
R52
K53
OapB-OLE* crystal form I
F
A504
G577
G578
G503
G501
R20
U499
C579
U502
K51
R49
R35
N56
N54
R52
U498
K53
OapB-OLE* crystal form II

Figure S2 (Previous Page). Electron density maps for OapB and OapB-OLE* complex structures. (*A–C*) Simulated annealing composite omit maps of (*A*) the OapB apo structure, (*B*) the OapB-OLE* complex structure from crystal form I, and (*C*) the OapB-OLE* complex structure from crystal form II contoured at 1.0 σ. The anomalous difference map (magenta mesh in (*B*)) contoured at 5.0 σ shows six cobalt (III) hexammine-binding sites in OLE* from the cobalt-derivative crystal in form I. (*D*) Superimposition of OapB-OLE* complex structures determined from crystal form I and form II. (*E* and *F*) OapB-OLE* interface of the complex structures determined from (*E*) crystal form I and (*F*) crystal form II, respectively. OLE* nucleotides and OapB amino acids at the protein-RNA interface are shown as sticks superimposed with the simulated annealing composite omit map contoured at 1.0 σ.

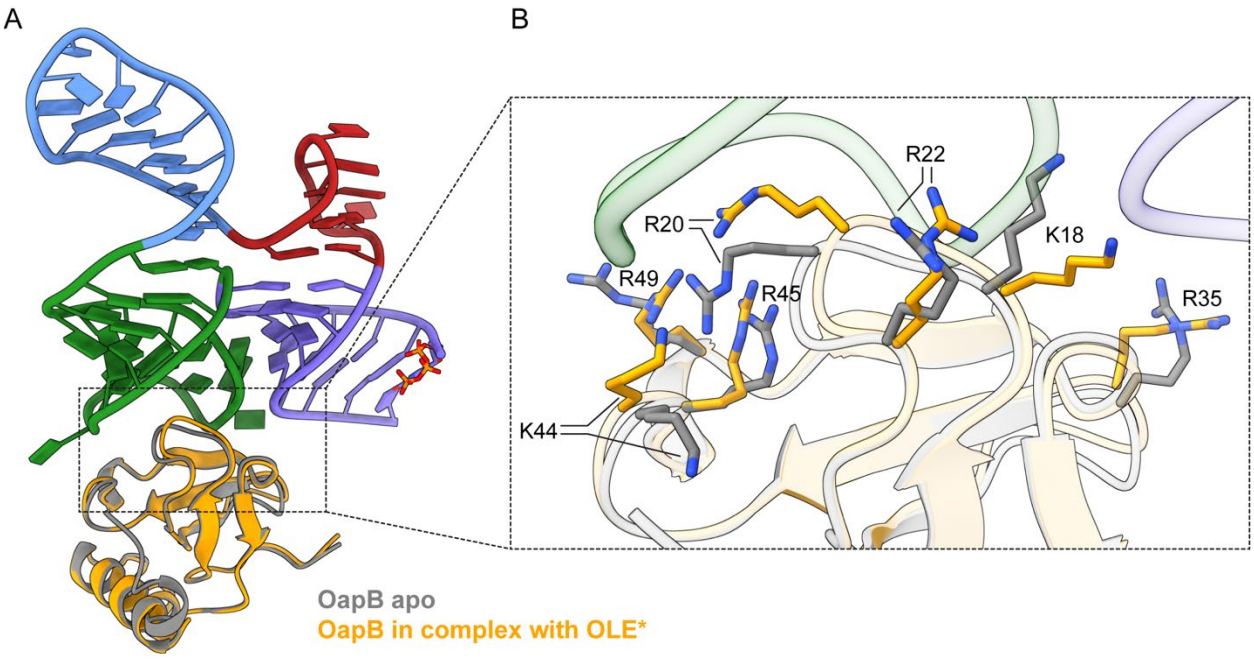

Figure S3. Conformational changes of OapB upon OLE RNA binding. (*A*) Superimposition of OapB apo and OapB-OLE* complex structures reveals notable conformational changes in several loops regions of OapB. (*B*) Expanded view of the conformational changes of OapB residues at the OLE RNA-binding interface.

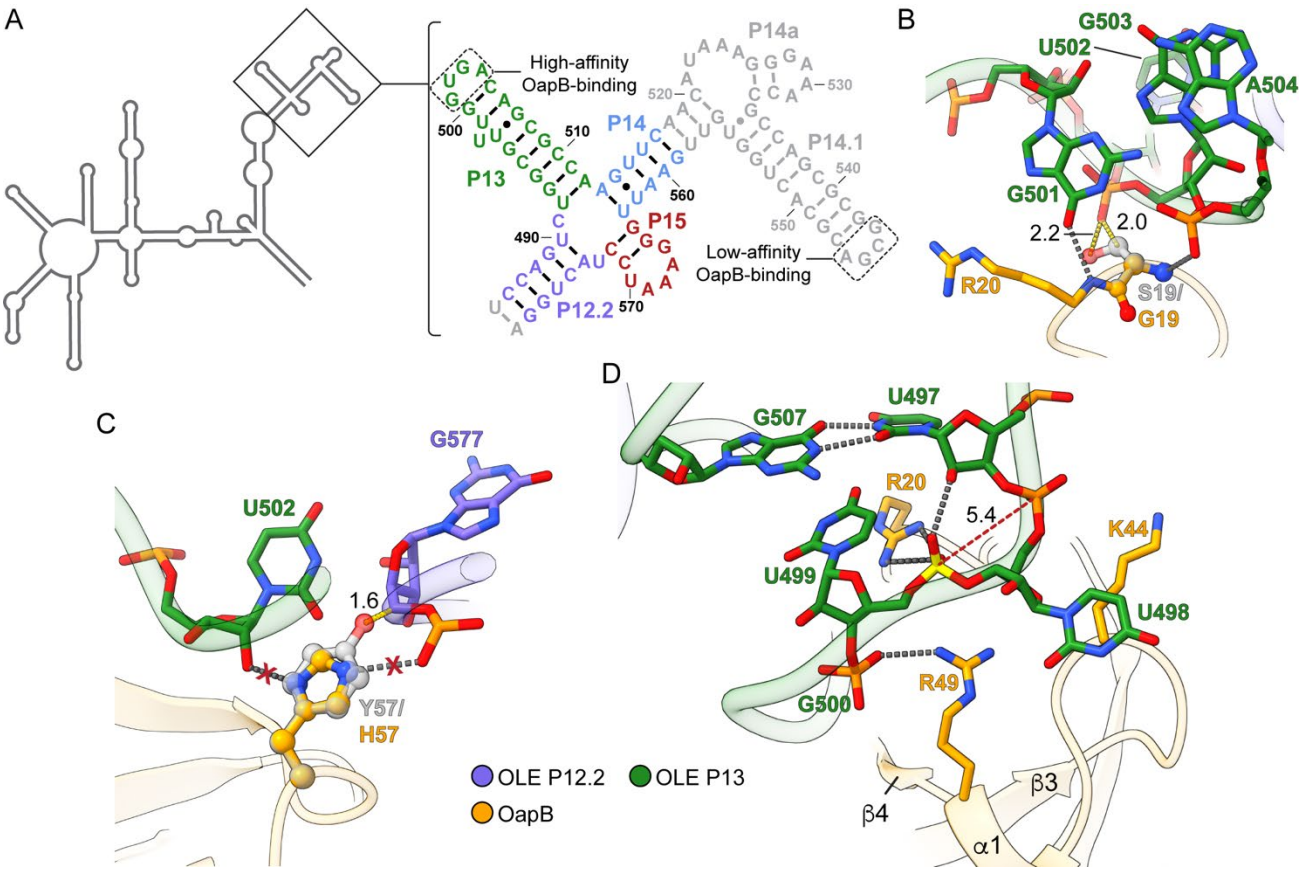

Figure S4. Molecular details of the OapB-OLE RNA interactions. (*A*) Sequence and secondary structure models of the OLE RNA substructure with two OapB binding sites. Nucleotides not present in the OLE* used for crystallization are shown as gray. (*B*) Modeling of the G19S mutation in the OapB-OLE* complex structure. G19 (orange) and S19 (transparent gray) are shown in ball-and-stick representation. Hydrogen bonds are shown as gray dashed lines. Potential steric clashes upon mutation are indicated by yellow dashed lines with distances indicated (in Å). (*C*) Modeling of the H57Y mutation in the OapB-OLE* complex structure. H57 (orange) and Y57 (transparent gray) are shown in ball-and-stick representation. Hydrogen bonds that would be lost due to H57Y mutation are labeled with red crosses. The potential steric clash upon mutation is indicated by yellow dashed lines with the distance indicated (in Å). (*D*) Detailed interactions around the bulged U498 region in crystal form II of the OapB-OLE* complex. The phosphate group connecting U498 and U499 is highlighted in yellow. The phosphate-to-phosphate distance between U498 and U499 is indicated (in Å) and labeled with a red dashed line.

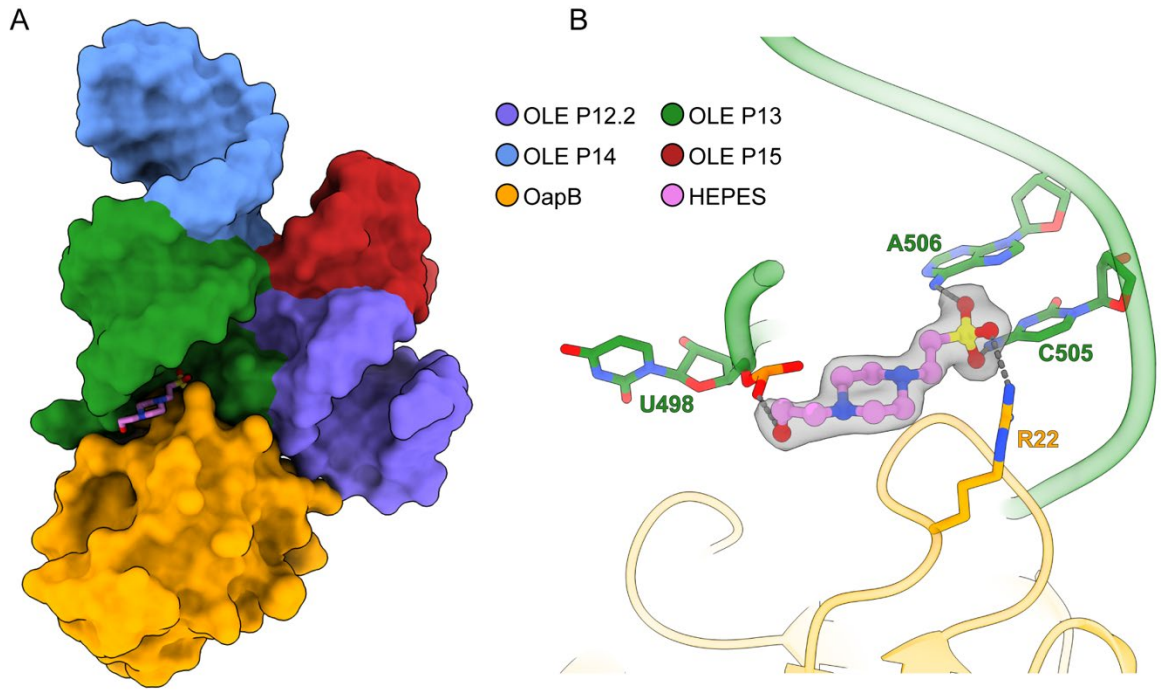

Figure S5. A possible metabolite-binding pocket in the OapB-OLE RNA complex. (*A*) A HEPES molecule is bound in a pocket at the OapB-OLE RNA interface. OapB and OLE RNA are shown as surfaces and the HEPES molecule is shown as sticks. (*B*) Close-up view of the HEPES binding site in OapB-OLE* complex structure. Hydrogen bonds are shown as gray dashed lines. The HEPES molecule is superimposed with mF_o–DF_c omit map contoured at 3.0 σ.

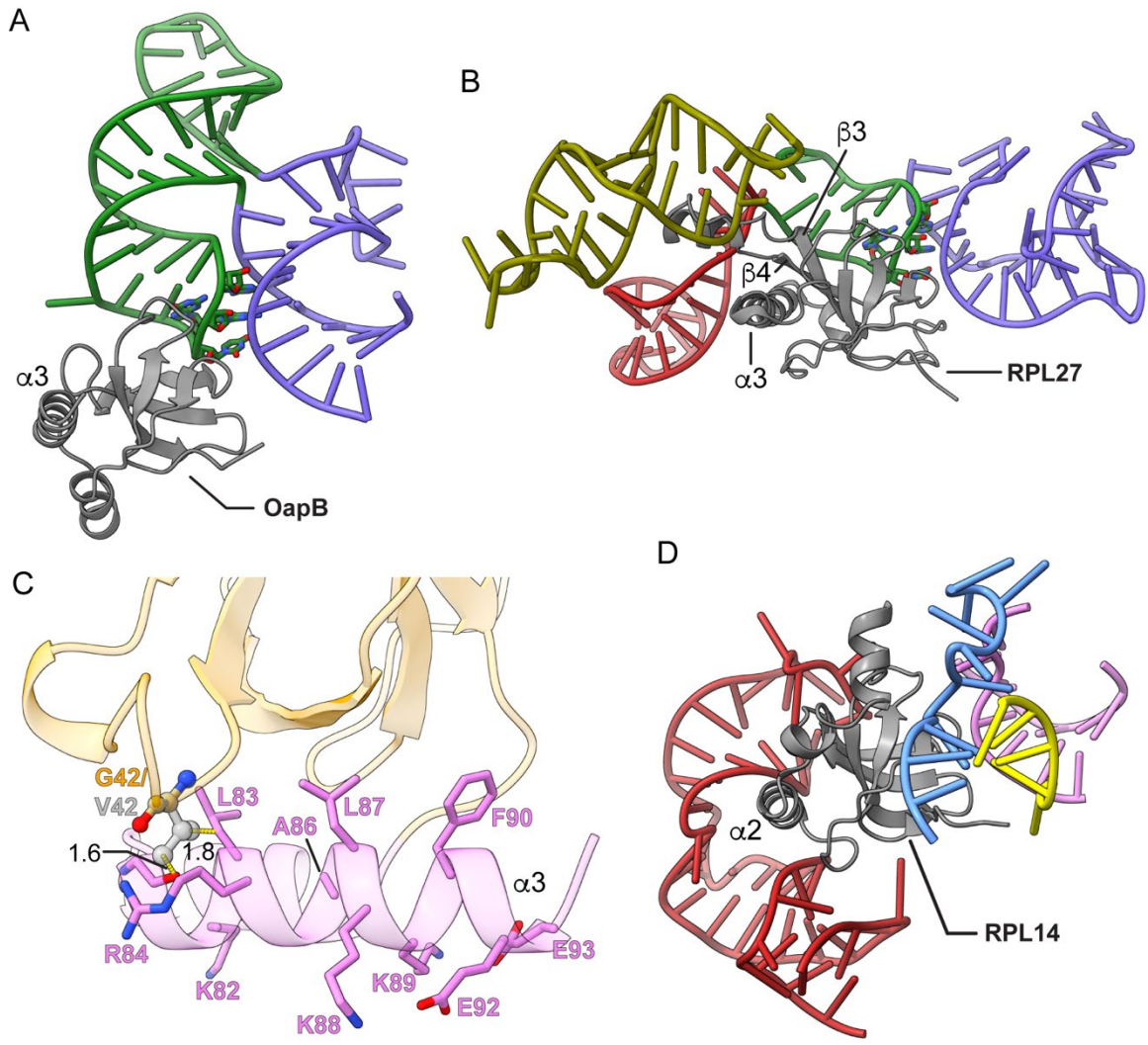

Figure S6. Structural comparisons of OapB with eukaryotic ribosomal proteins L27 and L14. (*A*) Arrangement of RNA and protein components of the OapB-OLE* complex. Nucleotides in the GUGA tetraloop of OLE stem P13 are shown as sticks. The two coaxial stacks of OLE*, both which make contacts with OapB, are colored in green and blue, respectively. (*B*) Arrangement of RNA and protein components of the RPL27 bound in the human 80S ribosome (PDB 6EK0). Four discontinuous 28S rRNA regions that contact RPL27 are depicted in different colors. Nucleotides in the GUAA tetraloop of 28S rRNA are shown as sticks. (*C*) Modeling of the G42V mutation in the OapB-OLE* complex structure. G42 (orange) and V42 (transparent gray) are shown in ball-and-stick representation. Potential steric clashes upon mutation are indicated by yellow dashed lines with distances indicated (in Å). Side chains of residues in OapB α3 are displayed to show the amphipathic nature of the helix. (*D*) Arrangement of RNA and protein components of RPL14 in the human 80S ribosome (PDB

6EK0). Four discontinuous 28S rRNA fragments that make contacts with RPL14 are depicted with different colors.

Table S1. X-ray crystallography data collection, phasing and refinement statistics

	OapB apo native (PDB 7K9B)	OapB apo I-derivative (PDB 7K9C)	OapB-OLE* complex native (Crystal form I) (PDB 7KKV)	OapB-OLE* complex Co-derivative (Crystal form I) (PDB 7K9D)	OapB-OLE* complex (Crystal form II) (PDB 7K9E)
Data collection					
Space group	$P\ 1\ 2_1\ 1$	$P\ 1\ 2_1\ 1$	$R\ 3\ 2$	$R\ 3\ 2$	$P\ 6_5$
Cell dimensions					
a, *b*, *c* (Å)	47.92, 34.91, 49.81	47.90, 34.91, 49.64	98.95, 98.95, 197.85	98.82, 98.82, 198.90	71.99, 71.99, 223.90
α, β, γ (°)	90, 90.24, 90	90, 90.151, 90	90, 90, 120	90, 90, 120	90, 90, 120
Wavelength (Å)	0.9792	0.8266	0.9791	1.6058	0.9792
Resolution (Å)	47.92–1.20 (1.245–1.20)*	49.64–1.00 (1.036–1.00)	41.87–2.00 (2.071–2.00)	41.83–2.098 (2.173–2.098)	54.47–2.10 (2.175–2.10)
R_{sym} or R_{merge}	0.034 (0.156)	0.062 (1.24)	0.028 (1.045)	0.046 (1.22)	0.044 (0.860)
I / σI	17.8 (5.1)	10.8 (1.1)	22.0 (1.6)	29.1 (1.7)	16.4 (1.2)
$CC_{1/2}$	0.999 (0.973)	0.998 (0.463)	1.000 (0.691)	0.998 (0.817)	0.999 (0.648)
Completeness (%)	98.3 (92.9)	96.4 (92.1)	98.9 (98.4)	99.7 (99.1)	99.2 (99.2)
Redundancy	3.3 (2.8)	4.2 (4.1)	4.5 (4.7)	9.6 (9.3)	3.5 (3.6)
Refinement					
Resolution (Å)	47.92–1.20 (1.245–1.20)	49.64–1.00 (1.036–1.00)	41.87–2.00 (2.071–2.00)	41.83–2.098 (2.173–2.098)	54.47–2.10 (2.175–2.10)
No. reflections	50646 (4788)	85600 (8113)	25242 (2472)	22151 (2149)	37854 (3791)
R_{work} / R_{free}	0.1231/0.1540 (0.1294/0.1725)	0.1494/0.1628 (0.2840/0.2817)	0.1711/0.1869 (0.3310/0.3318)	0.1659/0.2000 (0.3239/0.3593)	0.1731/0.2053 (0.3050/0.3597)
No. atoms					
Macromolecules	1751	1780	2022	2003	3953
Ligand/ion	2	17	57	97	64
Water	311	235	278	240	401
B-factors					
Macromolecules	14.17	13.17	75.87	72.00	69.88
Ligand/ion	14.16	20.48	79.89	89.04	84.33
Water	28.66	25.58	75.19	74.05	68.49
R.m.s deviations					
Bond lengths (Å)	0.011	0.011	0.004	0.002	0.006
Bond angles (°)	1.45	1.41	0.68	0.67	1.14
Validation					
MolProbity score	1.19	1.37	0.57	1.23	1.20
Clashscore	2.24	3.30	0.00	2.25	2.49
Poor rotamers (%)	0.00	0.00	0.00	0.00	0.00
Ramachandran plot					
Favored (%)	96.86	96.32	97.70	96.55	97.04
Allowed (%)	3.14	3.68	2.30	3.45	2.96
Disallowed (%)	0.00	0.00	0.00	0.00	0.00

*Values in parentheses are for highest-resolution shell.